ORIGINAL ARTICLE

Proteomic analysis of non-muscle invasive and muscle invasive bladder cancer highlights distinct subgroups with metabolic, matrisomal, and immune hallmarks and emphasizes importance of the stromal compartment

Thien-Ly Julia Dinh[1,2], Manuel Rogg[1], Miguel Cosenza-Contreras[1,2], Mujia Li[1,3], Max Zirngibl[1], Niko Pinter[1], Konrad Kurowski[1], Frank Hause[1,4,5], Lena Pauli[1], Fiona Imberg[1], Alana Huynh[1], Marlene Schmid[1], Ievgen Glavinsky[1], Luisa Braun[1], Clara Van Wymersch[1], Luise Bergmann[1], Xenia Ungefug[1], Marion Kunz[1], Tilman Werner[1,2,6], Patrick Bernhard[1,2,6], Guadalupe Espadas[7,8], Eva Brombacher[2,6,9,10], Julia Schueler[11], Eduard Sabido[7,8], Clemens Kreutz[9,10], Christian Gratzke[12], Martin Werner[1,13], Markus Grabbert[12], Peter Bronsert[1], Christoph Schell[1] and Oliver Schilling[1,13]*

[1] Institute for Surgical Pathology, Faculty of Medicine, Medical Center—University of Freiburg, University of Freiburg, Freiburg, Germany
[2] Faculty of Biology, University of Freiburg, Freiburg, Germany
[3] Institute of Pharmaceutical Sciences, University of Freiburg, Freiburg, Germany
[4] Department of Pharmaceutical Chemistry and Bioanalytics, Institute of Pharmacy, Martin Luther University Halle-Wittenberg, Halle, Germany
[5] Bellvitge Institute for Biomedical Research (IDIBELL), L'Hospitalet del Llobregat, Barcelona, Spain
[6] Spemann Graduate School of Biology and Medicine, Freiburg, Germany
[7] Centre for Genomic Regulation, Barcelona Institute of Science and Technology, Barcelona, Spain
[8] University Pompeu Fabra, Barcelona, Spain
[9] Institute of Medical Biometry and Statistics, Faculty of Medicine and Medical Center – University of Freiburg, Freiburg, Germany
[10] Centre for Integrative Biological Signalling Studies (CIBSS), University of Freiburg, Freiburg, Germany
[11] Charles River Laboratories Germany GmbH, Freiburg, Germany
[12] Department of Urology, Faculty of Medicine, Medical Center—University of Freiburg, University of Freiburg, Freiburg, Germany
[13] German Cancer Consortium and German Cancer Research Center, Heidelberg, Germany

*Correspondence to: O Schilling, Institute for Surgical Pathology, Faculty of Medicine, Breisacher Strasse 115a, 79106 Freiburg, Germany. E-mail: oliver.schilling@uniklinik-freiburg.de

Abstract

We present the proteomic profiling of 79 bladder cancers, including treatment-naïve non-muscle-invasive bladder cancer (NMIBC, $n = 17$), muscle-invasive bladder cancer (MIBC, $n = 51$), and neoadjuvant-treated MIBC ($n = 11$). Proteins were extracted from formalin-fixed, paraffin-embedded samples and analyzed using data-independent acquisition, yielding >8,000 quantified proteins. MIBC, compared to NMIBC, shows an extracellular matrix (ECM) and immune response signature as well as alteration of the metabolic proteome together with concomitant depletion of proteins involved in cell-cell adhesion and lipid metabolism. Neoadjuvant treatment did not consistently impact the proteome of the residual tumor mass. NMIBC presents two proteomic subgroups that correlate with histological grade and feature signatures of cell adhesion or lipid/DNA metabolism. Treatment-naïve MIBC presents three proteomic subgroups with resemblance to the basal-squamous, stroma-rich, or luminal subtypes and signatures of metabolism, immune functionality, or ECM. The metabolic subgroup presents an immune-depleted microenvironment, whereas the ECM and immune subgroups are enriched for markers of M2-like tumor-associated macrophages and dendritic cells. Markers for natural killer cells are exclusive for the ECM subgroup, and markers for cytotoxic T cells are a hallmark of the immune subgroup. Endogenous proteolysis is increased in MIBC alongside upregulation of matrix metalloproteases, including MMP-14. Genomic panel sequencing yielded the prototypical profile of prevalent *FGRF3* alterations in NMIBC and *TP53* alterations in MIBC. Tumor-stroma interactions of MIBC were investigated by proteomic analysis of patient-derived xenografts, highlighting specific tumor and stroma contributions to the matrisome and tumor-induced stromal proteome phenotypes.

© 2024 The Author(s). *The Journal of Pathology* published by John Wiley & Sons Ltd on behalf of The Pathological Society of Great Britain and Ireland.

Keywords: bladder cancer; proteomics; tumor microenvironment

Introduction

Urothelial bladder cancer ranks among the top 10 most common malignancies worldwide [1], comprising non-muscle-invasive bladder cancer (NMIBC, Tis to T1 stage) and muscle-invasive bladder cancer (MIBC, T2 to T4 stages) [2]. Progression from NMIBC to MIBC may occur [3]. Treatment of NMIBC includes transurethral resection (TURB) and intravesical chemotherapy (including Bacillus Calmette-Guérin) [4,5], while treatment of MIBC may require radical cystectomy (RCX) and potentially radiation therapy, (neo-)adjuvant chemotherapy, and/or immunotherapy [5,6]. Recurrence-free survival (RFS) and 5-year survival are substantially lower for MIBC than for NMIBC.

Transcriptomic and genomic studies have defined distinct bladder cancer (BC) subgroups [7–14], including the UROMOL classifier [8] for NMIBC and a consensus of six transcriptomic subtypes for MIBC [15]. However, the correlation between transcriptome and proteome data is limited [16,17]. At present, there exist only a few published proteomic studies focusing on BC [18–20]. We present the deep proteomic characterization of urothelial BC.

Materials and methods

Ethics and patient consent statement

The study was approved by the Ethics Board of the University Medical Center Freiburg (approval 491/16). Written patient consent was obtained before inclusion. The study is in accordance with the Declaration of Helsinki.

Patient cohort and tissue collection

We enrolled 79 patients with urothelial BC, operated at the University Medical Center Freiburg between 2015 and 2020, including 17 treatment-naïve NMIBC, 51 treatment-naïve MIBC, and 11 neoadjuvant-treated MIBC cases. NMIBC samples were collected through TURB or ureter resection, and MIBC samples were obtained by TURB or RCX. Further characteristics are shown in Figure 1A and supplementary material, Table S1.

Patient-derived xenografts

Formalin-fixed paraffin-embedded (FFPE) samples of patient-derived xenografts (PDX) of MIBC were provided by Charles River Laboratories, Freiburg, Germany (supplementary material, Table S2).

Sample preparation

FFPE slides were deparaffinized and macrodissected to obtain ~1 mm^3 of tissue. Protein extraction was performed as described elsewhere [21] and prepared using S-TRAP™ (ProtiFi, Fairport, NY, USA). Peptide samples were vacuum-concentrated until dry and stored at $-80\,^{\circ}C$.

Liquid chromatography–tandem mass spectometry (LC–MS/MS) and statistical analysis

Samples were analyzed using an Orbitrap Fusion Lumos mass spectrometer (Thermo Fisher Scientific, Bremen, Germany) coupled to an EASY-nLC 1200 (Thermo Fisher Scientific) in random order. A more detailed description of the LC–MS/MS measurements, processing of RAW files using DIA-NN (version 1.7.12) [22], and statistical analysis is given in Supplementary materials and methods [23–32].

Tumor-infiltrating lymphocytes

Tumor-infiltrating lymphocytes (TILs) were quantified by a trained pathologist using consensus scoring recommendations for breast cancer [33]. TILs were evaluated on FFPE tissue sections (4 μm) at ×200–400 magnification. Percentage stromal TILs represented mononuclear inflammatory cells in the stromal compartment. Exclusions included crush artifacts, necrotic areas, peritumoral follicular aggregates, and tertiary lymphoid structures.

Immunohistochemistry for Ki-67, MMP-14, BSCL-2, and YAP-1

Immunohistochemistry (IHC) was performed using FFPE tissue sections (4 μm) with the following primary antibodies: anti-Ki-67 [34] (Catalogue No. IR626, Agilent Dako, Santa Clara, CA, USA), anti-MMP-14 (Catalogue No. ab51074 [35], Aabcam, Cambridge, UK), anti-BSCL2 (Catalogue No. PA5-23621, Invitrogen, Carlsbad, CA, USA), or anti-YAP1 (Catalogue No. 14074 [36], Cell Signaling Technology, Danvers, MA, USA). Further details are specified in Supplementary materials and methods.

Multiplexed immunofluorescence staining of PD-L1 and CD8

Iterative indirect immunofluorescence imaging of FFPE tissue was performed as previously described [37]. The following antibodies were applied: AE1/AE3, CD3, CD4, CD8, PDCD1, PD-L1, Goat anti-Mouse IgG conjugated to Alexa Fluor 647, and Donkey anti-Rabbit IgG conjugated to Alexa Fluor 555. Hoechst 33342 was employed for counterstaining of nuclei (see Supplementary materials and methods).

For quantification of CD8 and PD-1 cells in PD-L1 low and high expressing tumors, QuPath image analysis software (version 0.2.1) was used for cell detection and identification of double-positive cells by thresholding [38]. Five cancer samples per PD-L1 group (high versus low), and three regions per sample were quantified (a total of 15 regions per group) and used for statistical analysis (unpaired Wilcoxon test).
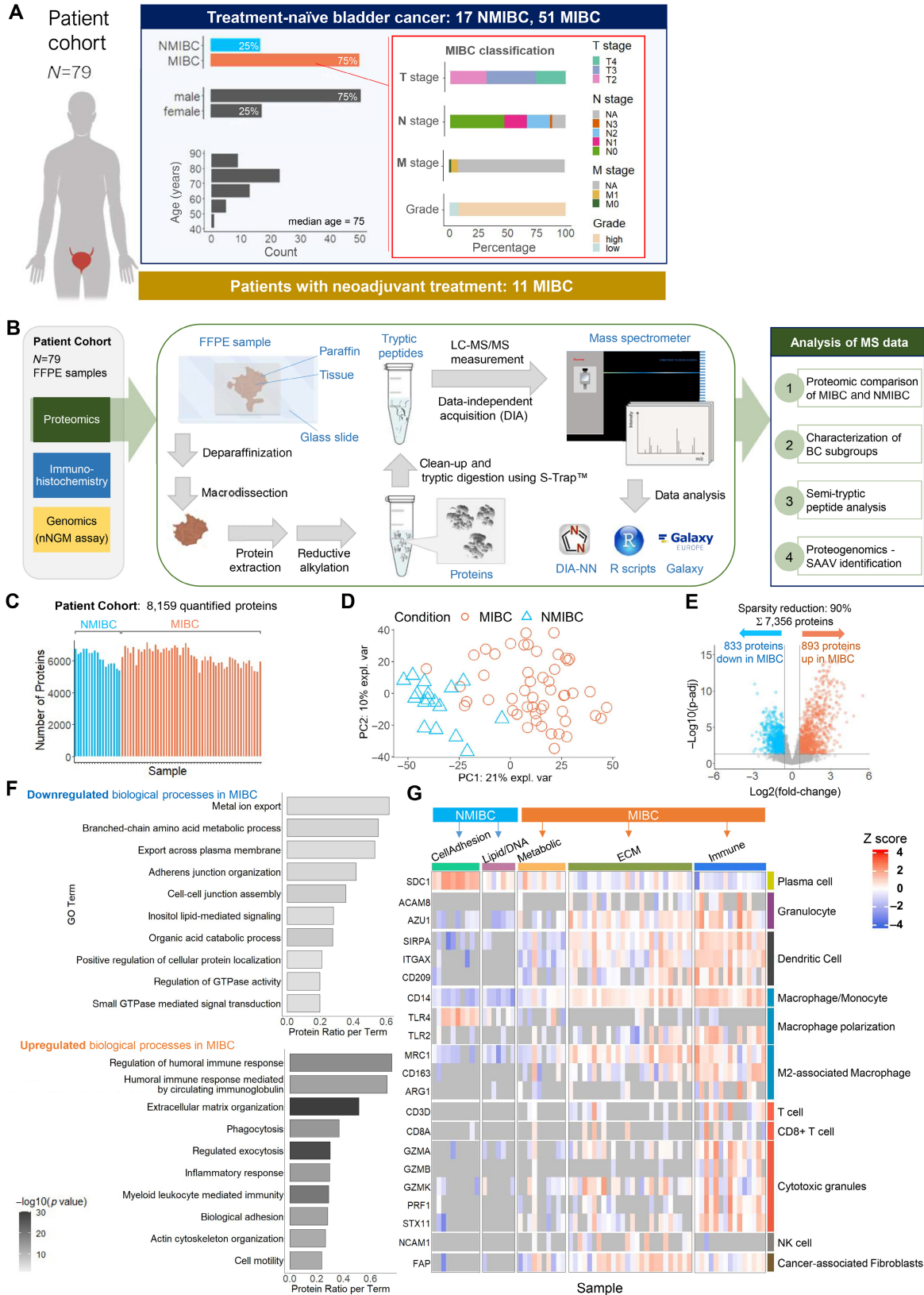
Figure 1. Overview of study. (A) Overview of BC cohort. (B) Overview of experimental workflow (created with Biorender.com). (C) Quantified proteins per sample. (D) Principal component analysis of treatment-naïve BC samples. (E) Differential abundance of proteins in treatment-naïve MIBC versus NMIBC at sparsity reduction with a 90% cutoff, resulting in 7,356 proteins. We used linear models of microarray analysis (LIMMA), applying a significance cutoff using a Benjamini–Hochberg adjusted p value (p-adj) < 0.05 and a minimal fold-change of 1.5. (F) Comparison of downregulated (top) or upregulated (bottom) biological processes in treatment-naïve MIBC versus NMIBC. (G) Immune and stromal cell markers across NMIBC and MIBC. The selected proteins shown are either significantly enriched/depleted (Fisher's exact test, $p < 0.05$) or differentially regulated (quantitative difference >1.5-fold-change and p-adj < 0.05) in at least one proteomic group. The Z score was calculated based on sample intensity subtracted by the mean intensity and divided by the standard deviation across all samples.

Sequencing panel – DNA isolation and measurement

DNA from FFPE specimens was extracted and analyzed according to the National Network Genomic Medicine (nNGM) panel Germany version 2.1. Gene list and details are specified in Supplementary materials and methods.

MMP-14 silencing

The human BC cell line T24 [39] (Catalogue No. 300352, CLS Cell Lines Service, Eppelheim, Germany) and HEK293T/17 cells [40] (Catalogue No. CRL-11268, ATCC, Manassas, VA, USA) were cultured as described [41]. shRNA experiments were carried out as described [41] using two MISSION® shRNA constructs targeting *MMP14* (Sigma-Aldrich, Taufkirchen, Germany): shMMP14_a (sh_A): TRCN0000050854 (sequence: CGGCCTTCTGTTCCTGATAAA), shMMP14_b (sh_B): TRCN0000050855 (sequence: CGATGA AGTCTTCACTTACTT). MISSION pLKO.1-puro vector (SHC002V) served as control (shCtrl). Stable cell lines were generated through a 7-day selection (1 µg/ml puromycin, InvivoGen, San Diego, CA, USA) and probed by immunoblotting [41]. Cell lines were mycoplasma-free and genotyped. Migration and invasion analysis employed 24-well plate 8-µm pore-size transwell inserts (Corning, Corning, NY, USA) (see also Supplementary materials and methods).

Results and discussion

Deep proteome coverage of bladder cancer

We investigated the proteome biology of urothelial BC together with genomic, histological, and immunohistochemical profiling (Figure 1A,B, supplementary material, Tables S1 and S3). Tumor tissue percentage within macrodissected samples in 10 selected cases was 82% ± 17% (94% ± 2% for NMIBC and 73% ± 17% for MIBC). Using data-independent acquisition (DIA), we identified 8,159 proteins at a 1% false discovery rate (FDR) based on 55,953 identified unique peptides with an average of 6,242 ± 499 proteins per sample (Figure 1C. These numbers are comparable to those obtained in emerging proteome studies on BC [19,20]. Protein intensities were symmetrically and near-normally distributed with a wide dynamic range (supplementary material, Figure S1A).

NMIBC and MIBC differed in their proteome alongside enrichment of an immune- and matrisome-related proteome in MIBC

The proteomes of treatment-naïve MIBC and NMIBC showed good segregation by principal component analysis (PCA) (Figure 1D) and sparse partial least-squares discriminant analysis (sPLS-DA) (supplementary material, Figure S1B). Over 20% of the identified proteome differed significantly between treatment-naïve MIBC and NMIBC, with 893 upregulated and 833 downregulated proteins (Figure 1E), illustrating highly differing proteome biology (supplementary material, Table S4).

There was an enrichment of extracellular matrix (ECM) and immune response proteins in treatment-naïve MIBC versus NMIBC (Figure 1F), including proteins of the complement system, the kallikrein-kinin system (supplementary material, Figure S2), and key proteins for antigen presentation (e.g. HLA-DR/-DQ/-DP). Despite variations in standard surgical procedures for sample collection between MIBC and NMIBC, these findings align with prior comparative studies [18,42]. MIBC was enriched in proteins that regulate integrin signaling (e.g. fermitin family members 1/2/3) and proteins related to focal adhesion biology such as focal adhesion kinase 1 (supplementary material, Figure S3).

Our deep proteome coverage included marker proteins for tumor-infiltrating immune and stromal cells (Figure 1G). The cancer-associated fibroblast (CAF) marker FAPα distinguished between NMIBC and MIBC. The tumor microenvironment (TME) of NMIBC tended to have fewer immune cells compared to MIBC, with reduced levels of most immune cell markers (Figure 1G). NMIBC showed some macrophages/monocytes (marker: CD14). The TLR4 to TLR2 ratio in NMIBC was shifted toward TLR4 (Figure 1G), indicating M1 polarization [43], while MIBC was characterized by markers for M2 polarization [43] (Figure 1G). In summary, NMIBC and MIBC presented divergent TMEs.

The metabolic proteome differed between NMIBC and MIBC, with MIBC presenting a likely decreased lipid metabolism (supplementary material, Table S4). Transcription factors with roles in metabolic reprogramming, such as peroxisome proliferator-activated receptor gamma (PPARG), were depleted in MIBC (supplementary material, Table S4), underlining a metabolic shift in MIBC, in line with previous reports [18,44].

Proteins linked to the ubiquitin-dependent endoplasmic reticulum-associated protein degradation (ERAD) pathway wee upregulated in MIBC, e.g. derlin-1 (supplementary material, Figure S4), possibly linked to accumulated misfolded proteins in the secretory pathway in MIBC [45].

Our cohort included an additional 11 neoadjuvant-treated MIBC cases with chemotherapy or instillation therapy. Proteome profiles of neoadjuvant-treated MIBC closely mapped to the proteomes of treatment-naïve MIBC (supplementary material, Figure S5), suggesting comparable proteome biology. However, this result might have been affected by the small cohort size.

NMIBC proteomes revealed two subgroups representing cell-adhesion or lipid-metabolism biology

Unsupervised hierarchical clustering of NMIBC proteomes identified two distinct subgroups (Figure 2A), with
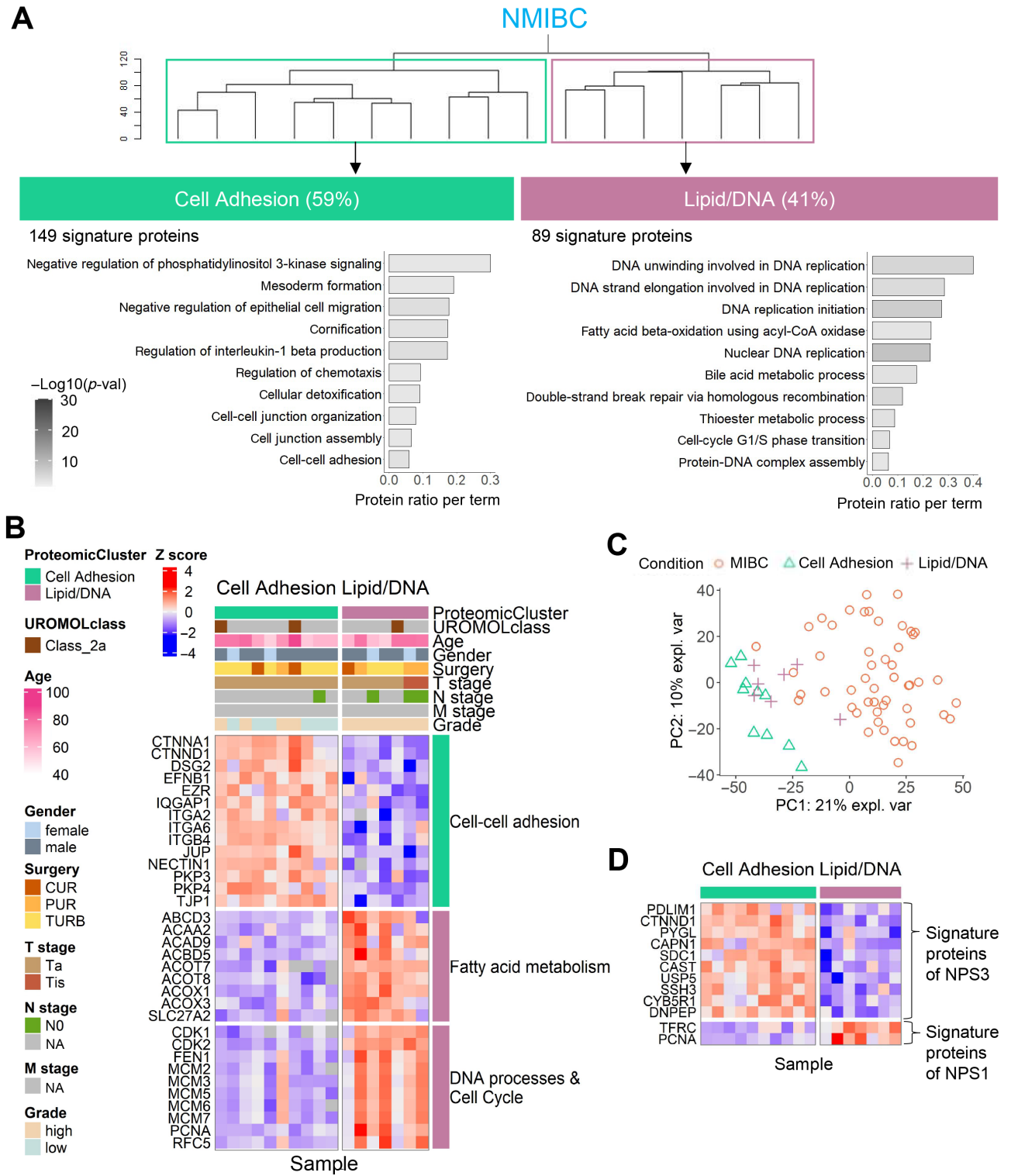
Figure 2. Proteomic characterization of NMIBC. (A) Unsupervised hierarchical clustering analysis with Euclidean distance and Ward's minimum variance method of NMIBC identified two distinct clusters. The analysis was performed after sparsity reduction to max. 25%, leaving 4,800 proteins in the dataset, and solely on NMIBC samples. (B) Heatmap of selected differentially regulated proteins in proteomic NMIBC subgroups. Only two proteomes were classifiable into one of the UROMOL subtypes [8]. CUR, complete ureter resection; PUR, partial ureter resection. (C) Principal component analysis of NMIBC subgroups and MIBC. The Z score was calculated based on sample intensity subtracted by the mean intensity and divided by the standard deviation across all samples. (D) Comparison of our NMIBC subgroups with proteomic subtypes of Stroggilos et al [19]. The Cell Adhesion subgroup is enriched with 10 signature proteins of the NPS3 group.

linear models of microarray analysis (LIMMA) yielding significantly enriched proteins (>1.5-fold-change, p-adj < 0.05) (Figure 2B, supplementary material, Table S5).

One subgroup was enriched in cell-adhesion proteins and the other in lipid-metabolism and DNA-replication proteins. We named the subgroups accordingly. The MIBC

proteome was closer to the Lipid/DNA subgroup than to the Cell Adhesion subgroup (Figure 2C). The Cell Adhesion subgroup contained all low-grade NMIBC cases, in contrast to the Lipid/DNA subgroup (Figure 2B, Fisher's exact test, $p = 0.035$).

Stroggilos *et al* [19] identified three NMIBC proteome subgroups (NPS1/2/3). NPS1 features cell-cycle enrichment, NPS2 parallels NPS1 but adds an EMT/ECM signature and decreased CD47. NPS3 was enriched in cell–cell adhesion and luminal traits, tied to low-grade disease. Ten NPS3 signature proteins matched our Cell Adhesion subgroup for low grade (Figure 2D). Two NPS1 signature proteins aligned with our Lipid/DNA cluster (Figure 2D), and both were enriched for cell-cycle proteins. Application of the UROMOL classifier [8] to our proteome data showed insignificant association ($p > 0.05$, Figure 2B, supplementary material, Table S5), likely due to limited mRNA-protein correlation [16,17], akin to previous findings [19]. Due to the lack of sufficient follow-up data for NMIBC cases, we were unable to assess whether the proteome subgroups of NMIBC were associated with differences in disease progression.

MIBC proteomes revealed three proteome subgroups with matrisomal, metabolic, or immune hallmarks and differential abundance of therapeutic targets

Unsupervised hierarchical clustering identified three proteome subgroups for MIBC (Figure 3A), with LIMMA highlighting enriched proteins (p-adj < 0.05; quantitative difference >1.5-fold-change). The three subgroups were characterized by metabolic, matrisomal/ECM, or immune hallmarks (Figure 3A,B). We detected enriched luminal markers in the metabolic subgroup including GATA3, FOXA1, uroplakin 2 [10,46], while basal markers [12] were particularly enriched in the immune subgroup (e.g. CD44). The ECM subgroup showed intermediate levels of both luminal and basal markers (supplementary material, Table S6).

Xu *et al* [18] identified proteome-based subgroups in NMIBC and MIBC (UI to UIII). The UI subgroup contained both NMIBC (30/37) and MIBC (7/37) and had luminal traits. Our ECM subgroup resembled UIII with ECM and complement system proteins. The immune subgroup showed similarities to UII with cell-cycle, DNA-repair/replication proteins, and T-cell infiltration, yet basal markers have been reported for UIII, which has an ECM fingerprint.

Resemblance of our proteomic subgroups to transcriptome-based MIBC subgroups (consensusMIBC classifier [15]) was probed. Results matched well (Fisher's exact test, $p = 5.2 \times 10^{-9}$), aligning ECM subtype with stroma-rich, immune subtype with basal-squamous, and metabolic subtype with luminal subtypes (supplementary material, Table S6, supplementary material, Figure S6).

Although not statistically significant, the metabolic subgroup presented a higher proportion of T2 stage cases (Figure 3C). Of 51 treatment-naïve MIBC cases, 46 were accompanied by follow-up data with a median coverage of 350 days after surgery (Figure 3D); five M1 cases were excluded. Cox proportional hazard analysis highlighted T4 stage as being associated with shorter RFS, while the proteomic subgroups did not show differences (Figure 3E).

Proteomic BC subgroups showed varying therapy target levels. Immune therapy targets were found primarily in the immune subgroup (see the corresponding section below). Nectin-4 was reduced in the ECM and immune subgroups compared to the metabolic subgroup and NMIBC (Figure 3F, supplementary material, Figure S7). Some individual cases had notably elevated levels, suggesting the potential for personalized therapies. The ECM subgroup exhibited higher levels of ephrin receptor A2 (EPHA2), considered for antibody drug conjugate-type therapies in BC [47]. Our xenograft dataset (see below) further highlighted the tumor-cell located EPHA2. FAPα was particularly enriched for MIBC (Figure 1G), investigated as radioligand target for diagnostic [48] and therapeutic [49] use.

Fibroblast growth factor receptor 3 (FGFR3) was observed in several cases of the metabolic MIBC subgroup and the NMIBC cell-adhesion subgroup (Figure 3F), and FGFR3 inhibitors have been tested in clinical trials [50]. HER2 (ERBB2) showed reduced levels in the ECM and immune subgroups, with individual outliers (Figure 3F, supplementary material, Figure S7) and HER2-targeting therapies also undergoing clinical trials in BC [51,52]. Likewise, individual cases showed elevated EGFR levels. CDK4 was slightly enriched in the metabolic and immune subgroups, while CDK6 was enriched in the immune subgroup (Figure 3F, supplementary material, Figure S7), coinciding with elevated levels of the cell proliferation marker Ki67 (MKI67). CDK4/6 inhibitors have been discussed as a therapeutic approach for advanced BC [53].

ECM subgroup characterized by matrisomal proteins and dampened DNA damage response proteins

The ECM subgroup comprised 50% of the MIBC cases in our cohort. It presented intermediate levels of luminal [12,54–56] and basal markers [12,57] (Figure 3B). The gene ontology (GO) term 'extracellular matrix organization' failed to adequately represent the different aspects of ECM constituents summarized by the matrisome classification [58]. We applied the matrisome classification to our proteome data and noticed that the ECM subgroup was particularly enriched for the core matrisome, including collagens, proteoglycans, and glycoproteins (Figure 3G). An additional hallmark of the ECM subgroup is enrichment of proteins linked to the complement and coagulation system (Figure 3B, supplementary material, Figure S8).

We examined our proteomic data for immune cell markers (Figure 1G). In the ECM subgroup, we noticed elevated levels of CD14 and CD280, which suggested the presence of M2-like tumor-associated macrophages (TAMs) [59,60]. The markers CD11c, signal regulatory
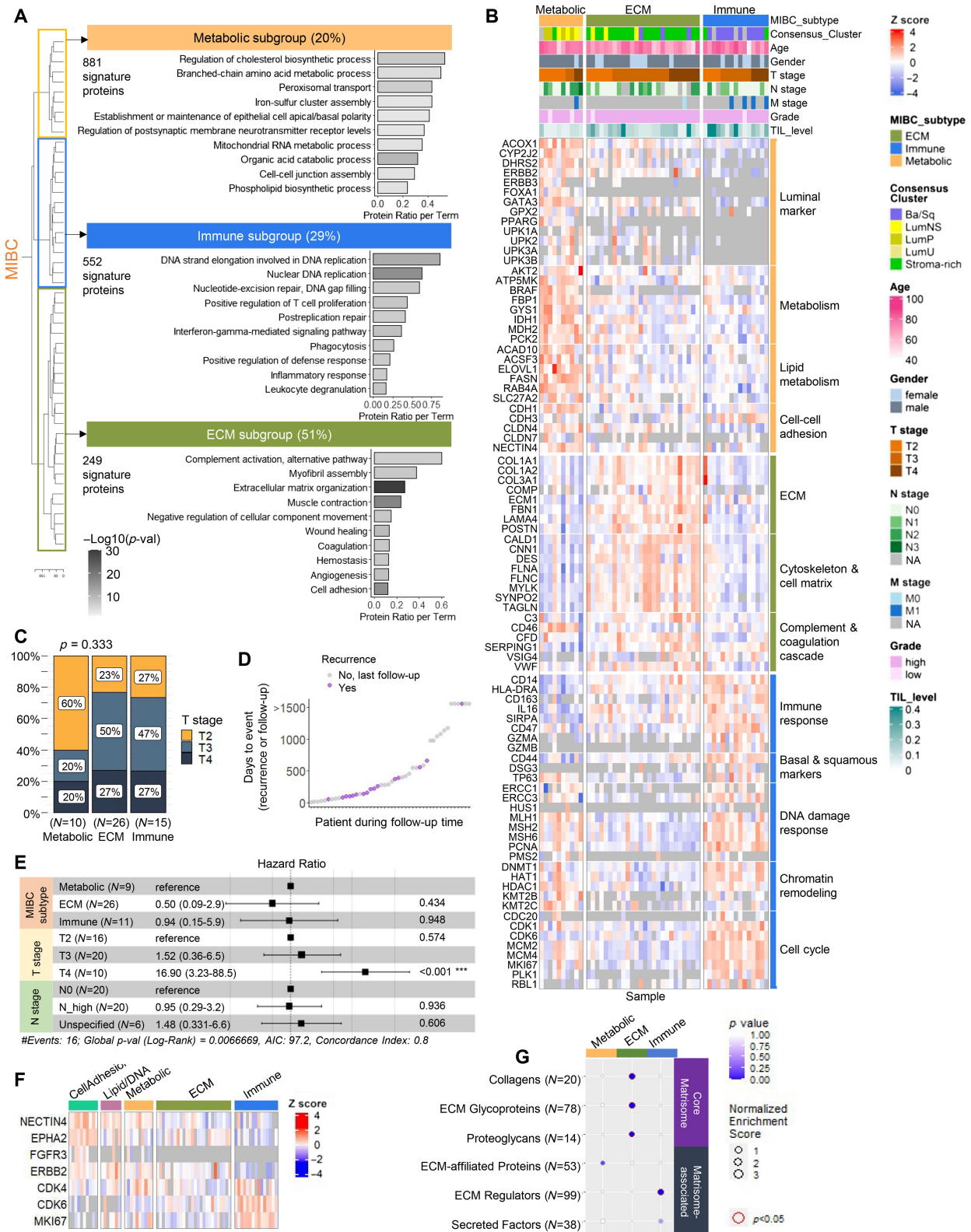
Figure 3. Proteomic characterization of MIBC. (A) Unsupervised hierarchical clustering of MIBC proteomes (proteins: quantitative difference >1.5- fold-change and *p*-adj < 0.05) performed after sparsity reduction to maximum 25%, leaving 4,800 proteins in the dataset, and solely on MIBC samples. (B) Heatmap including previously established candidates for molecular characterization of MIBC [9,15]. Proteins were enriched/depleted (Fisher's exact test, *p* < 0.05) or differentially regulated (*p*-adj < 0.05) in one or more proteomic MIBC subgroup. Neuroendocrine markers were not enriched in any subtype. The *Z* score was calculated based on sample intensity subtracted by the mean intensity and divided by the standard deviation across all samples. (C) Distribution of samples across proteomic MIBC subgroups, based on T stage. (D) Distribution of recurrence-free survival or follow-up time, respectively. Five cases presented with recurrent tumor or metastasis during surgery and were removed from this analysis. (E) Cox proportional hazard analysis. (F) Heatmap of possible therapeutic targets. FGFR3 intensities were taken from an additional analysis using a library-predicted approach and are specifically enriched in the metabolic subgroup of MIBC (Fisher's exact test, $p = 8 \times 10^{-4}$). (G) Enrichment of matrisome proteins across proteomic MIBC subgroups.

protein alpha (SIRPA), and CD209 pointed to dendritic cells [61], while CD66B and azurocidin 1 (AZU1) were indicative of granulocytes [62,63]. The ECM subgroup featured enrichment of NCAM1, a marker for NK cells [64], but largely lacked cytotoxic T-cell markers (CD8A, CD3D), granzyme B, and perforin-1.

The ECM subgroup featured enriched markers for CAFs, including FAPα and PDGFRβ (Figure 1G). Extracellular components and infiltration of CAFs indicated a TME with increased stiffness. Mechanical stress may activate HIPPO-YAP1 signaling [65]. We used YAP1 IHC, which suggested YAP1 was more prominent in MIBC tumor cells compared to NMIBC cells, particularly in the ECM and immune subgroups (Figure 4A,B). However, there was no correlation between nuclear YAP1 levels and advanced T stage in MIBC [66] (Fisher's exact test, $p = 0.52$). We evaluated the transcriptional activity of YAP by analyzing its associated proteins [67,68]. Most showed no significant differences between BC subtypes or were undetected (supplementary material, Figure S9). Hence, we refrained from making assumptions about YAP's net transcriptional activity. In contrast to the other MIBC subgroups, proteins involved in DNA replication and damage response were downregulated in the ECM subgroup [e.g. MCM component 3/4/7, DNA polymerase subunits, Ki-67 (Figure 3B, supplementary material, Table S6)].

Metabolic subgroup was enriched for proteins involved in lipid metabolism but depleted for immune-related features

The metabolic subgroup featured luminal markers [12,69] (Figure 3B). It contained >800 signature proteins (>1.5-fold-change, *p*-adj < 0.05). Many of these had enzymatic activity and were involved in energy metabolism (citric acid cycle, oxidative phosphorylation). Numerous signaling/regulatory kinases and phosphatases featured prominently in this subgroup (e.g. SRC). A prominent signature of the metabolic subgroup is lipid metabolism (Figure 3A), including fatty acid oxidation (e.g. fatty acid synthase) and corresponding transcription factors such as PPARG (Figure 3B, supplementary material, Table S6). The metabolic subgroup featured reduced levels of immune cell markers (Figure 1G), indicative of an immune-depleted TME.

Characterization of immune-enriched subgroup

The immune subgroup was enriched for basal/squamous markers (e.g. CD44 [12,57]) (Figure 3B) with concomitant loss of luminal markers (e.g. uroplakin 2, GATA3, PPARG [12,54–56]) (*p*-adj < 0.05). This subgroup featured CD3D and CD8A, signaling the presence of cytotoxic T cells (Figure 1G), together with an enrichment of granzymes A/B/K and perforin (Fisher's exact test, $p < 0.05$) (Figure 1G). Other immune cell markers point to dendritic cells (CD11c, integrin alpha-X [61]), granulocytes (CD66B, AZU1 [63]), and M2-like TAMs

(e.g. CD14, CD280, CD163, CD206 [18,60,70]). Proteins involved in antigen presentation were enriched, including MHC type I and II, corroborating the presence of professional antigen-presenting cells such as dendritic cells. The NK-cell marker CD56 (NCAM1) and proteins of the complement system were depleted (Figures 1G and 3B).

The immune subgroup was also enriched for the proinflammatory interleukin-18, which stimulates interferon-gamma production [71,72], alongside an enrichment of proteins that are linked to interferon signaling (e.g. interferon-induced protein 35) (supplementary material, Table S6). DNA replication and repair proteins formed another signature of the immune subgroup (Figure 3B) including Ki-67 (Figure 3B, supplementary material, Figure S10A), for which IHC highlighted strong expression by tumor cells (supplementary material, Figure S10B) and enrichment in the immune subgroup (supplementary material, Figure S10C).

Genomic profiling highlighted prototypical profile of *FGFR3* mutations for NMIBC and *TP53* mutations for MIBC

We performed genomic profiling for 65 of the 68 treatment-naïve BC samples using the nNGM panel assay (version 2.1) with 27 pan-cancer markers (supplementary material, Table S7). Missense mutations were prominent, followed by nonsense mutations (Figure 4C). Deletions and insertions were relatively rare. The most frequent mutations were found in *FGFR3* and *TP53* [9,73]. Next, we focused on mutations that exhibited predicted or annotated pathogenicity together with different prevalence in NMIBC or MIBC (Figure 4D). We observed at least one *FGFR3* mutation in 90% of cases within the Cell Adhesion subgroup of NMIBC ($p = 5.8 \times 10^{-7}$), contrasting with the absence of such mutations in the Lipid/DNA subgroup. A similar trend emerged for *PIK3CA* mutations, with 40% observed in the Cell Adhesion subgroup compared to only 17% in the Lipid/DNA subgroup ($p = 0.026$). *TP53* mutations were depleted in the Cell Adhesion subgroup of NMIBC ($p = 0.034$) and were enriched particularly in the Immune subgroup of MIBC ($p = 0.033$).

We aimed to probe for proteome-level sequence alterations [e.g. single amino acid variants (SAAVs)] that were not covered by the reference UniProt proteome sequence used for peptide-spectrum matching (PSM) of our mass spectrometry data. Without considering putative pathogenicity, our genomic data revealed 93 coding single-nucleotide polymorphisms (SNPs), five amino acid deletions, nine terminations/truncations, and four frameshifts. We determined the theoretical proteomic detectability of these genomic variants by focusing on corresponding tryptic peptides of seven to 30 amino acid length and mapping to proteins that were proteomically detected based on additional consensus sequence peptides. This resulted in 57 tryptic variant peptides for SAAVs, three tryptic variant peptides representing amino acid deletions, and five tryptic
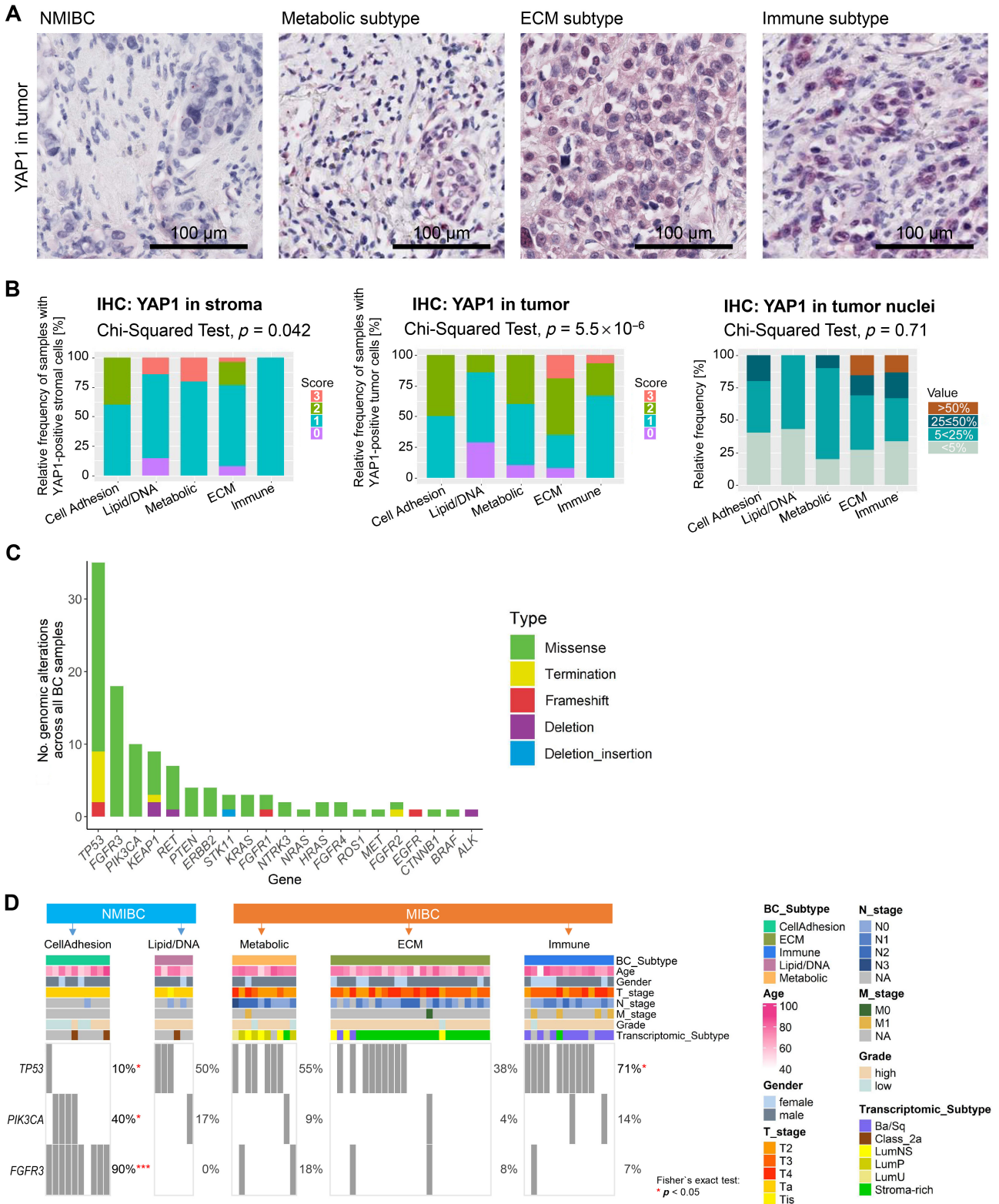
Figure 4. YAP1 staining; genomic characterization of cohort. (A) IHC of YAP1 in treatment-naïve BC (NMIBC, $n = 17$; MIBC, $n = 50$) comparing differences across MIBC subtypes and NMIBC. (B) Quantification of YAP1 in different tumor areas. YAP1 intensity score of 0 represents no signal, and a score of 3 indicates high signal intensity. Chi-squared tests show a correlation between YAP1 and BC subclusters in both stroma (left) and tumor (middle). The right panel depicts the percentage of tumor nuclei with positive YAP1 signal. (C) Count and types of genomic alterations per gene. (D) Frequency of genes with likely pathogenic mutations (FATHMM [74], ClinVar [75]) and different prevalence in BC subgroups (Fisher's exact test, $p < 0.05$).

variant peptides representing sequence terminations. This theoretical overview highlights the perspective of proteogenomics, i.e. the proteomic corroboration

of genomic alterations. However, proteogenomic analyses (based on the aforementioned tryptic variant peptide sequences added to the reference proteome
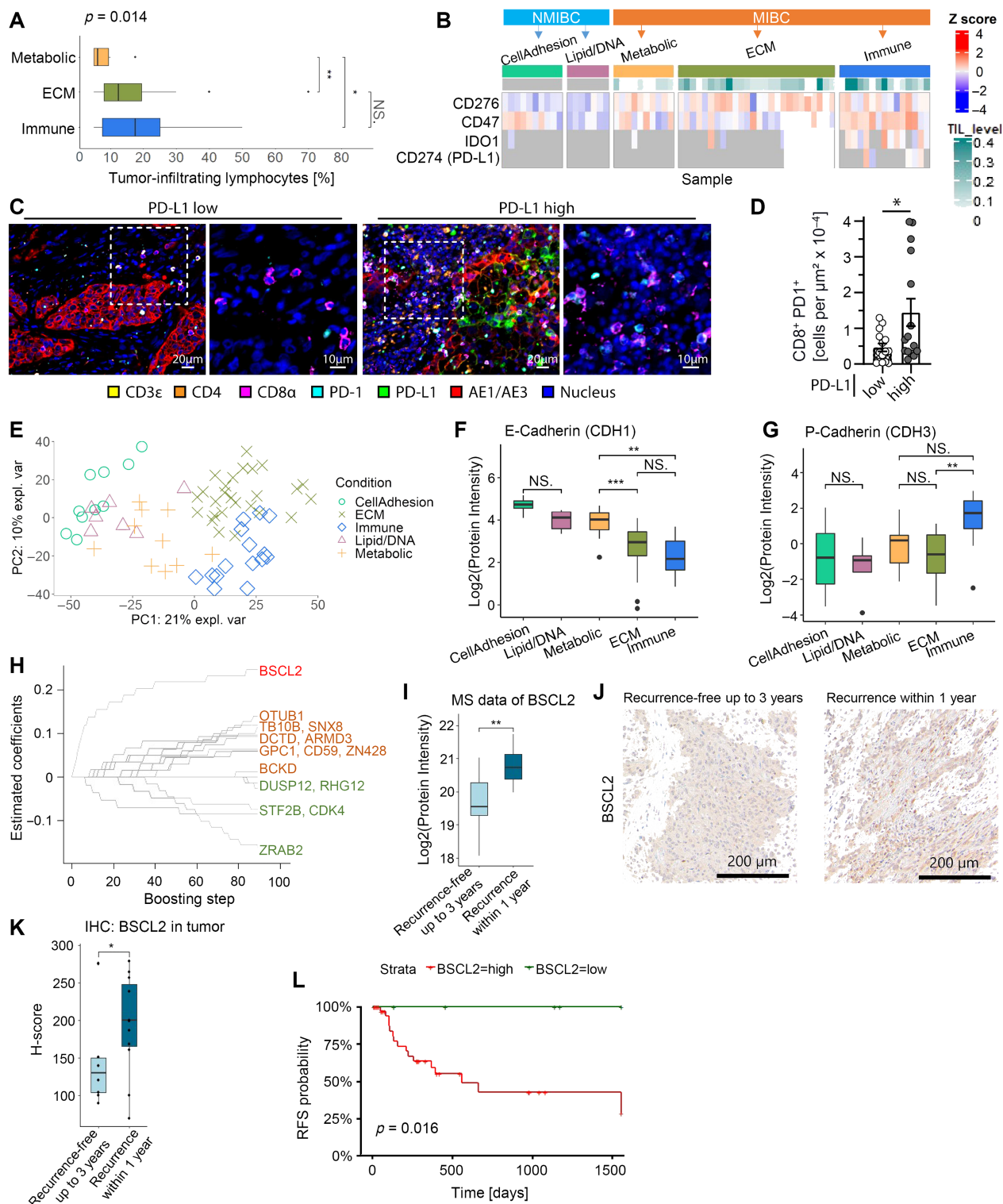
Figure 5. Tumor–infiltrating immune cells in MIBC; association of BSCL2 with recurrence-free survival. (A) Fraction of tumor–infiltrating lymphocytes in MIBC subgroups (Kruskal–Wallis test, *$p = 0.014$), given in [%] as intratumoral stromal area occupied by mononuclear inflammatory cells over total intratumoral stromal area. (B) Differential regulation of immune checkpoint proteins. PD-L1 intensities were taken from the library-predicted approach (Fisher's exact test, $p = 1.3 \times 10^{-3}$). (C) Representative images of CD8 (pink) and PD1 (turquoise) in MIBC with either high or low PD-L1 (green) ($n = 10$) and (D) quantitative data (*$p = 0.045$, unpaired Wilcoxon test). The bar plot shows the mean of cells per μm^2, error bars represent SEM. (E) Principal component analysis of proteomic BC subgroups. (F and G) Mass spectrometric intensities of E- and P-cadherin in proteomic BC subgroups (E-cadherin: $p = 1.9 \times 10^{-9}$; P-Cadherin: $p = 1.3 \times 10^{-3}$, ANOVA). (H) Proteins associated with time to recurrence. (I) MS intensities of BSCL2 comparing recurrence within 1 year ($n = 11$) to cases with recurrence-free survival for more than 3 years ($n = 8$) (*$p = 0.007$, one-sided *t*-test; results of two-sided *t*-test are given in supplementary material, Figure S13). (J) Representative IHC of BSCL2. (K) IHC quantification (h-score [83]) comparing recurrence within 1 year ($n = 11$) to cases with recurrence-free survival for more than 3 years ($n = 8$) ($p = 0.045$, one-sided *t*-test; results of two-sided *t*-test are given in supplementary material, Figure S13). (L) Kaplan–Meier plot of BSCL2 ($p = 0.016$, log-rank test). Cutoff point was determined by maximally selected rank statistics [80]. Vertical lines indicate censored data.
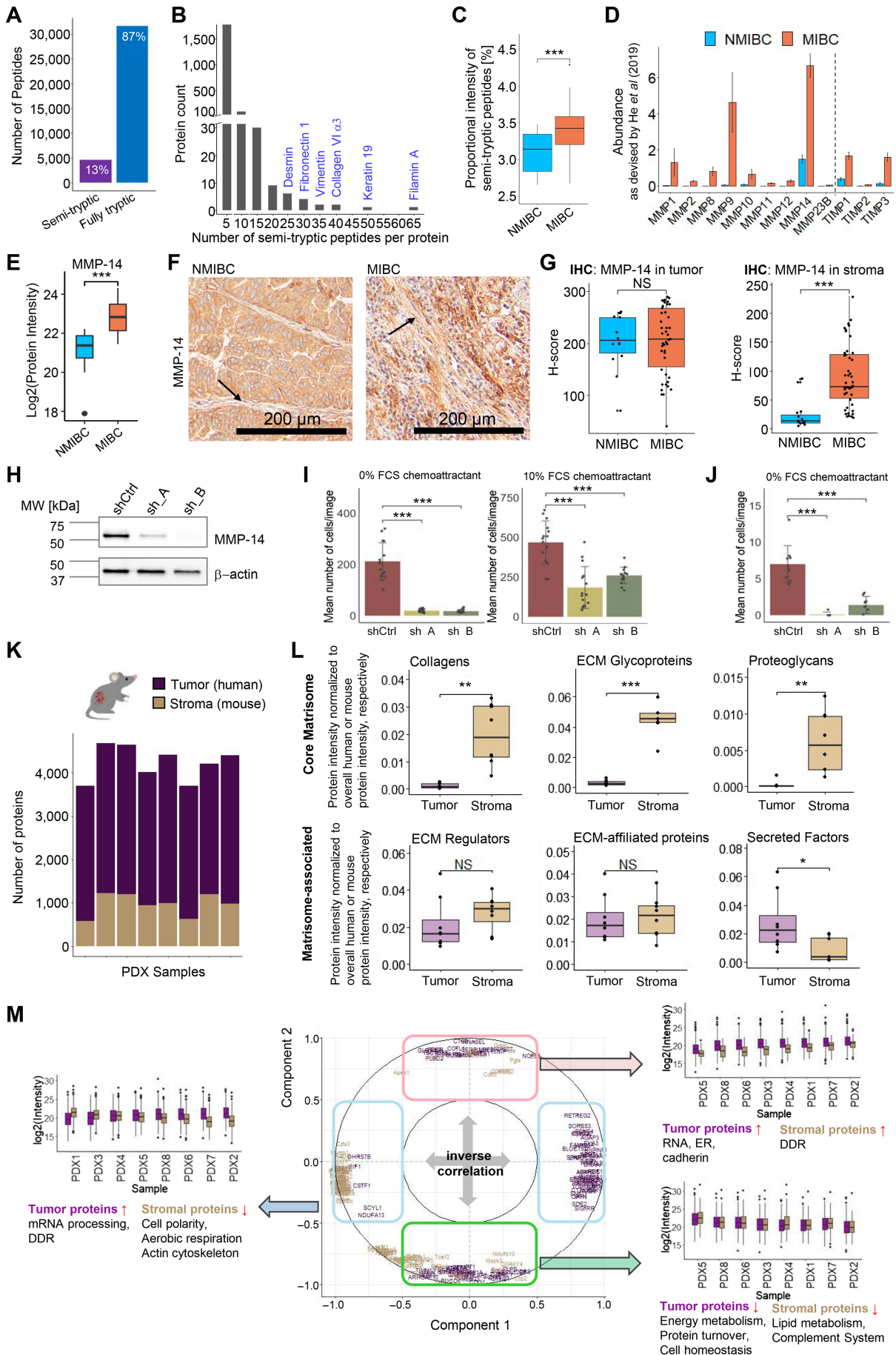
Figure 6 Legend on next page.

sequence) of the present data yielded the proteomic corroboration of only one variant (KRAS G12D) in one MIBC sample (not shown). This limited outcome highlights the need for improved sequence coverage in MS-based proteomics to exploit fully the possibilities of proteogenomic corroboration.

Immune cell infiltration in MIBC

We histologically assessed immune cell infiltration in MIBC. TILs correlated with the subgroups (Figure 5A). Immune-depleted luminal subgroup aligned with luminal features [44,56], while high immune infiltration characterized the basal-squamous subgroup [44,56]. No significant correlations were found with gender, age, TNM, or grade (Kruskal–Wallis test, $p > 0.05$).

In MIBC, we detected the immune checkpoint proteins CD276, CD47, and IDO-1 (Figure 5B) with elevated presence in one or several MIBC subgroups compared to NMIBC, suggesting an immunosuppressive TME (Figure 1G). IDO-1 has been associated with tryptophan metabolism, leading to its replacement by phenylalanine in protein translation via WARS-1 [76]. Despite an enrichment of IDO-1 and WARS-1 in the immune subgroup, we did not observe increased W>F substitutions (supplementary material, Figure S11).

We employed a predicted spectral library for an additional analysis to capture proteins that are possibly underrepresented in the pooled reference sample. We identified additional cytokines (e.g. CXCL16) and immune checkpoint proteins, notably PD-L1 solely in the immune subgroup (Figure 5B, supplementary material, Figure S12). PD-1 remained undetected by LC–MS/MS and immunostaining (not shown), indicating its absence in most MIBC samples. For 10 selected MIBC samples, we pursued multiplexed immunostaining analysis of PD-1, PD-L1, and CD8 (Figure 5C,D). Three different regions were analyzed in each sample, yielding 30 analyses. CD8$^+$ cells that concomitantly express PD-1 were detected in only a very few regions. Moreover, these cases were constrained to PD-L1$^+$ MIBCs.

The metabolic MIBC subgroup showed proteomic proximity to NMIBC

The metabolic subgroup displayed proteomic proximity to NMIBC (Figure 5E). This resemblance extended to the levels of cadherins across BC subtypes (Figure 5F,G), for which a switch from E-cadherin in NMIBC to P- (or N-) cadherin has been reported as MIBC progresses in grade and stage [77].

Elevated BSCL2 levels are associated with shortened RFS in MIBC

We used the CoxBoost method [78] to identify proteins with prognostic value (Figure 5H). Seipin (BSCL-2) had the largest estimated coefficient and was associated with shorter PFS in early boosting steps. BSCL2 is a transmembrane protein of the endoplasmic reticulum associated with lipid droplet formation [79]. Reduced BSCL2 levels were detected for patients with prolonged PFS (Figure 5I, supplementary material, Figure S13). IHC showed that BSCL2 was present mainly in tumor cells (Figure 5J) and corroborated elevated BSCL2 levels in cases with early recurrence (Figure 5K). Kaplan–Meier analysis supports an association of BSCL2 with RFS (Figure 5L). Analysis of Human Protein Atlas [81] data for BSCL2 with KMPlot [82] and using auto-selection for optimal cutoff resulted in a log-rank p value of 0.022 and hazard ratio of 1.36 for elevated BSCL2 levels.

MIBC presented elevated endogenous proteolytic processing

To capture endogenous proteolytic processing (supplementary material, Figure S14A), we analyzed the present dataset with a spectral library representing semi-tryptic and tryptic peptide sequences, identifying more than 4,600 semi-tryptic peptides (Figure 6A). Over 1,500 proteins were found with at least one event of proteolytic processing (Figure 6B, supplementary material, Table S8). More than 20 proteolytic events were found for a small group of proteins (Figure 6B). The elevated

Figure 6. Elevated proteolysis and MMP levels in MIBC; proteomic characterization of MIBC PDX models. (A) Number of semi-tryptic peptides and fully tryptic peptides in treatment-naïve cases. (B) Number of semi-tryptic peptides per protein. (C) Proportional intensity of semi-tryptic peptides in MIBC and NMIBC ($p = 3.2 \times 10^{-5}$, t-test). (D) Mean abundance of MMPs and TIMPs [86] (error bars represent SD). (E) MMP-14 levels ($p = 6.0 \times 10^{-6}$, t-test). (F) Representative MMP-14 IHC. The arrows highlight staining in stromal regions. (G) IHC quantification (h-score [83]) of MMP-14 in tumor and stroma of treatment-naïve bladder cancer (NMIBC, $n = 11$; MIBC, $n = 46$; $p = 7.9 \times 10^{-6}$ unpaired Wilcoxon rank-sum test). (H) Immunoblot of T24 cells with shRNA-based knockdown of MMP-14 using two different constructs (sh_A and sh_B) and scrambled control (shCtrl). (I) Transwell migration (mean number of cells, ±SD) of T24 cells bearing MMP-14 shRNA-knockdown versus control with 0% or 10% FCS chemoattractant [left panel; shCtrl versus sh_A ($p = 2.8 \times 10^{-6}$, t-test) or sh_B ($p = 2.7 \times 10^{-5}$); right panel; shCtrl versus sh_A ($p = 6.1 \times 10^{-8}$) or sh_B ($p = 5.4 \times 10^{-8}$)]. Ten images were taken per condition. (J) Transwell matrigel invasion assay (mean number of cells, ±SD) of T24 cells bearing MMP-14 shRNA-knockdown versus control with 0% FCS chemoattractant, shCtrl versus sh_A ($p = 1.1 \times 10^{-5}$, t-test), and shCtrl versus sh_B ($p = 2.9 \times 10^{-5}$, t-test). The bar plot shows the mean of 10 images for each condition. (K) Mass spectrometry-based proteomics of the MIBC PDX specimens showing numbers of identified human (tumor) and murine (stroma) proteins per sample. (L) Summed protein intensities of either human (tumor) or mouse (stroma) origin for core matrisome (top) or matrisome-associated (bottom) proteins; *$p < 0.05$; **$p < 0.01$; ***$p < 0.001$; NS, not significant (t-test). (M) Cross-species correlation analysis of PDX proteomics data using a partial least-squares (PLS) model and depicted as a correlation circle plot, highlighting four distinct sets of proteins and displaying the corresponding top 100 proteins of human or murine origin. Box-and-whisker plots show summed protein intensities of tumor and stroma proteins of three differentially colored sets, highlighting their direct or inverse correlation. Key biological features of tumor and stroma proteins are stated.

level of semi-tryptic proportional intensities in MIBC compared to NMIBC (Figure 6C) indicated an increase in endogenous proteolytic processing regardless of the proteomic MIBC subgroup (supplementary material, Figure S14B).

Upregulation of matrix metalloproteases exceeded upregulation of tissue inhibitors of metalloproteases in MIBC

Matrix metalloproteases (MMPs) in BC increase with grade and invasiveness [84,85]. We found upregulation of several MMPs (1, 2, 8, 9, 10, 11, 12, 14, 23B) and their endogenous inhibitors TIMP-1 and TIMP-3 in MIBC (Figure 6D), raising the question of their stoichiometry. We employed the approach of He *et al* [86] to compare protein levels from DIA data. The combined MMP levels exceeded the combined TIMP levels, suggesting the presence of noninhibited MMPs. MMP-9 and MMP-14 (Figure 6E,F) were enriched in every MIBC subgroup (supplementary material, Figure S14C,D). Since both proteases surpassed the combined TIMP level, we did not consider in further detail that TIMP-1 and TIMP-3 had slightly different inhibitory profiles. We used IHC to investigate MMP-14, observing strong staining in the tumor cells of both NMIBC and MIBC samples, with significantly higher levels in the stromal cells of MIBC (Figure 6G). MMP-14 is a key mediator for the migratory and invasive behavior of T24 MIBC tumor cells [87], which we corroborated through stable silencing and assessing BC cell migration and invasion (Figure 6H–J, supplementary material, Figure S14E–G).

Proteome profiling of patient-derived xenografts of MIBC tumor–stroma correlations

To study tumor-stroma interactions, we analyzed a small cohort of MIBC PDX models ($n = 8$). We identified an average of 3,849 ± 192 tumor (human) and 1,283 ± 266 stromal (murine) proteins per sample (Figure 6K, supplementary material, Table S3). The core matrisome was predominantly of stromal origin (Figure 6L). Tumor- and stroma-derived ECM regulators and ECM-affiliated proteins were present at comparable levels (Figure 6I). Tumor-derived 'secreted factors' were more prominent than stromal-derived factors, e.g. proteins of the S100 family (supplementary material, Table S3). The core and affiliated matrisome aligned with the proteomic MIBC subgroups, where the core matrisome typified the ECM subgroup, while the affiliated matrisome was enriched in the metabolic and immune subgroups. Our findings emphasize the contribution of CAFs to the dominant ECM subgroup of MIBC, alongside tumor-autonomous biological processes.

Furthermore, we observed strong coregulation between tumor and stroma, with 1,638 tumor proteins and 970 stroma proteins interrelated and separated into four sets by two sPLS-DA components (supplementary material, Table S3). We focused on the top 100 proteins from both tumor and stroma (Figure 6M). An inverse correlation was observed between opposing protein sets, while proteins within the same set showed a positive correlation. For example, tumor proteins associated with energy metabolism, protein turnover, and cellular homeostasis correlated with stromal proteins linked to lipid transport and the complement system (Figure 6M, supplementary material, Figure S15).

Given the intertumor heterogeneity of the PDX models while the recipient mice were isogenic, the data illustrated induction of stromal heterogeneity by tumor heterogeneity.

Conclusions

We presented one of the first proteomic characterizations of NMIBC and MIBC using DIA with a deep proteome coverage of more than 8,000 quantified proteins. We identified two NMIBC subgroups that correlated with histological grade and three MIBC subgroups that correlated with the consensus subgroups: basal-squamous, luminal, and stroma-rich. MIBC subgroups differed in cell proliferation, ECM production, fatty acid metabolism, immune response, and both level and composition of infiltrated stromal cells. BSCL2 has been identified as a potential prognostic marker, as its elevated levels associate with a higher likelihood of tumor recurrence. We detected higher levels of proteolytic cleavage products in MIBC. Moreover, several MMPs were upregulated, including MMP-14, which promotes both invasiveness and migration of tumor cells. Mixed-species proteome profiling of MIBC PDX models enabled a closer inspection of tumor–stroma correlations.

Acknowledgements

Author contributions statement

PB, CS and OS designed the study. T-LJD, MR, ML, MZ, KK, LP, FI, AH, MS, IG, LBr, CVW, LBe, XU, MK, TW, PB, GE, JS and ES generated and collected data. CG and MG contributed patient data. T-LJD, MR, MC-C, NP, FH, EB, CK, PB, CS and OS performed data analysis and statistics. T-LJD, MR, MW, CS and OS performed data interpretation. All authors contributed to the writing of the manuscript and agreed to the final version of the manuscript.

Data availability statement

The raw files were uploaded to the European Genome-Phenome Archive (EGA). Data for the genomic experiment can be accessed using the EGA-ID EGAD00001010899; data for the proteomic experiment at EGAD0001000251; the proteomic experiment of MIBC PDXs at EGAD00010002512 and for the general study at EGAS00001007290. As patient-centric proteomic data are increasingly regarded as sensitive, personal data, EGA requires adherence to a data access agreement. The data access agreement for this dataset corresponds to the 'Harmonised Data Access Agreement (hDAA) for Controlled Access Data' brought forward by the European standardization framework for data integration and data-driven *in silico* models for personalized medicine – EU-STANDS4PM. The peptide and protein abundance matrices are available as supplementary material, Table S3.

References

1. Ferlay J, Colombet M, Soerjomataram I, *et al*. Cancer statistics for the year 2020: an overview. *Int J Cancer* 2021; **149**: 778–789.

2. Cumberbatch MGK, Jubber I, Black PC, *et al*. Epidemiology of bladder cancer: a systematic review and contemporary update of risk factors in 2018. *Eur Urol* 2018; **74**: 784–795.

3. Sylvester RJ, van der Meijden APM, Oosterlinck W, *et al*. Predicting recurrence and progression in individual patients with stage Ta T1 bladder cancer using EORTC risk tables: a combined analysis of 2596 patients from seven EORTC trials. *Eur Urol* 2006; **49**: 466–477.

4. Babjuk M, Burger M, Capoun O, *et al*. European Association of Urology guidelines on non-muscle-invasive bladder cancer (Ta, T1, and carcinoma in situ). *Eur Urol* 2022; **81**: 75–94.

5. Kaufman DS, Shipley WU, Feldman AS. Bladder cancer. *Lancet* 2009; **374**: 239–249.

6. Witjes JA, Bruins HM, Cathomas R, *et al*. European Association of Urology guidelines on muscle-invasive and metastatic bladder cancer: summary of the 2020 guidelines. *Eur Urol* 2021; **79**: 82–104.

7. Hedegaard J, Lamy P, Nordentoft I, *et al*. Comprehensive transcriptional analysis of early-stage urothelial carcinoma. *Cancer Cell* 2016; **30**: 27–42.

8. Lindskrog SV, Prip F, Lamy P, *et al*. An integrated multi-omics analysis identifies prognostic molecular subtypes of non-muscle-invasive bladder cancer. *Nat Commun* 2021; **12**: 2301.

9. Robertson AG, Kim J, Al-Ahmadie H, *et al*. Comprehensive molecular characterization of muscle-invasive bladder cancer. *Cell* 2017; **171**: 540–556.e25.

10. Damrauer JS, Hoadley KA, Chism DD, *et al*. Intrinsic subtypes of high-grade bladder cancer reflect the hallmarks of breast cancer biology. *Proc Natl Acad Sci U S A* 2014; **111**: 3110–3115.

11. Rebouissou S, Bernard-Pierrot I, Reyniès A d, *et al*. EGFR as a potential therapeutic target for a subset of muscle-invasive bladder cancers presenting a basal-like phenotype. *Sci Transl Med* 2014; **6**: 244ra91.

12. Choi W, Porten S, Kim S, *et al*. Identification of distinct basal and luminal subtypes of muscle-invasive bladder cancer with different sensitivities to frontline chemotherapy. *Cancer Cell* 2014; **25**: 152–165.

13. Marzouka N-A-D, Eriksson P, Rovira C, *et al*. A validation and extended description of the Lund taxonomy for urothelial carcinoma using the TCGA cohort. *Sci Rep* 2018; **8**: 3737.

14. Mo Q, Nikolos F, Chen F, *et al*. Prognostic power of a tumor differentiation gene signature for bladder urothelial carcinomas. *J Natl Cancer Inst* 2018; **110**: 448–459.

15. Kamoun A, Reyniès A d, Allory Y, *et al*. A consensus molecular classification of muscle-invasive bladder cancer. *Eur Urol* 2020; **77**: 420–433.

16. Liu Y, Beyer A, Aebersold R. On the dependency of cellular protein levels on mRNA abundance. *Cell* 2016; **165**: 535–550.

17. Fortelny N, Overall CM, Pavlidis P, *et al*. Can we predict protein from mRNA levels? *Nature* 2017; **547**: E19–E20.

18. Xu N, Yao Z, Shang G, *et al*. Integrated proteogenomic characterization of urothelial carcinoma of the bladder. *J Hematol Oncol* 2022; **15**: 76.

19. Stroggilos R, Mokou M, Latosinska A, *et al*. Proteome-based classification of nonmuscle invasive bladder cancer. *Int J Cancer* 2020; **146**: 281–294.

20. Valdés A, Bitzios A, Kassa E, *et al*. Proteomic comparison between different tissue preservation methods for identification of promising biomarkers of urothelial bladder cancer. *Sci Rep* 2021; **11**: 7595.

21. Fröhlich K, Brombacher E, Fahrner M, *et al*. Benchmarking of analysis strategies for data-independent acquisition proteomics using a large-scale dataset comprising inter-patient heterogeneity. *Nat Commun* 2022; **13**: 2622.

22. Demichev V, Messner CB, Vernardis SI, *et al*. DIA-NN: neural networks and interference correction enable deep proteome coverage in high throughput. *Nat Methods* 2020; **17**: 41–44.

23. Chiva C, Olivella R, Borràs E, *et al*. QCloud: a cloud-based quality control system for mass spectrometry-based proteomics laboratories. *PLoS One* 2018; **13**: e0189209.

24. Escher C, Reiter L, MacLean B, *et al*. Using iRT, a normalized retention time for more targeted measurement of peptides. *Proteomics* 2012; **12**: 1111–1121.

25. Cox J, Hein MY, Luber CA, *et al*. Accurate proteome-wide label-free quantification by delayed normalization and maximal peptide ratio extraction, termed MaxLFQ. *Mol Cell Proteomics* 2014; **13**: 2513–2526.

26. Ritchie ME, Phipson B, Di W, *et al*. Limma powers differential expression analyses for RNA-sequencing and microarray studies. *Nucleic Acids Res* 2015; **43**: e47.

27. Alexa A, Rahnenführer J, Lengauer T. Improved scoring of functional groups from gene expression data by decorrelating GO graph structure. *Bioinformatics* 2006; **22**: 1600–1607.

28. Kanehisa M. Toward understanding the origin and evolution of cellular organisms. *Protein Sci* 2019; **28**: 1947–1951.

29. Zhao Z, Zucknick M, Aittokallio T. EnrichIntersect: an R package for custom set enrichment analysis and interactive visualization of intersecting sets. *Bioinform Adv* 2022; **2**: vbac073.

30. Halstenbach T, Nelson K, Iglhaut G, *et al.* Impact of peri-implantitis on the proteome biology of crevicular fluid: a pilot study. *J Periodontol* 2023; **94**: 835–847.

31. Werner J, Bernhard P, Cosenza-Contreras M, *et al.* Targeted and explorative profiling of kallikrein proteases and global proteome biology of pancreatic ductal adenocarcinoma, chronic pancreatitis, and normal pancreas highlights disease-specific proteome remodelling. *Neoplasia* 2023; **36**: 100871.

32. Rohart F, Gautier B, Singh A, *et al.* mixOmics: an R package for omics feature selection and multiple data integration. *PLoS Comput Biol* 2017; **13**: e1005752.

33. Salgado R, Denkert C, Demaria S, *et al.* The evaluation of tumor-infiltrating lymphocytes (TILs) in breast cancer: recommendations by an international TILs working group 2014. *Ann Oncol* 2015; **26**: 259–271.

34. Metzger E, Stepputtis SS, Strietz J, *et al.* KDM4 inhibition targets breast cancer stem-like cells. *Cancer Res* 2017; **77**: 5900–5912.

35. Sántha P, Lenggenhager D, Finstadsveen A, *et al.* Morphological heterogeneity in pancreatic cancer reflects structural and functional divergence. *Cancers (Basel)* 2021; **13**: 895.

36. Zhang Y, Zegers MMP, Nagelkerke A, *et al.* Tunable hybrid matrices drive epithelial morphogenesis and YAP translocation. *Adv Sci (Weinh)* 2021; **8**: 2003380.

37. Rogg M, Maier JI, van Wymersch C, *et al.* α-Parvin defines a specific integrin adhesome to maintain the glomerular filtration barrier. *J Am Soc Nephrol* 2022; **33**: 786–808.

38. Bankhead P, Loughrey MB, Fernández JA, *et al.* QuPath: open source software for digital pathology image analysis. *Sci Rep* 2017; **7**: 16878.

39. Alfano M, Nebuloni M, Allevi R, *et al.* Linearized texture of three-dimensional extracellular matrix is mandatory for bladder cancer cell invasion. *Sci Rep* 2016; **6**: 36128.

40. Sena-Esteves M, Saeki Y, Camp SM, *et al.* Single-step conversion of cells to retrovirus vector producers with herpes simplex virus-Epstein-Barr virus hybrid amplicons. *J Virol* 1999; **73**: 10426–10439.

41. Stillger MN, Chen C-Y, Lai ZW, *et al.* Changes in calpain-2 expression during glioblastoma progression predisposes tumor cells to temozolomide resistance by minimizing DNA damage and p53-dependent apoptosis. *Cancer Cell Int* 2023; **23**: 49.

42. Silva TA, Azevedo H. Comparative bioinformatics analysis of prognostic and differentially expressed genes in non-muscle and muscle invasive bladder cancer. *J Proteomics* 2020; **229**: 103951.

43. Sauer R-S, Hackel D, Morschel L, *et al.* Toll like receptor (TLR)-4 as a regulator of peripheral endogenous opioid-mediated analgesia in inflammation. *Mol Pain* 2014; **10**: 10.

44. Tate T, Xiang T, Wobker SE, *et al.* Pparg signaling controls bladder cancer subtype and immune exclusion. *Nat Commun* 2021; **12**: 6160.

45. Nie Z, Chen M, Wen X, *et al.* Endoplasmic reticulum stress and tumor microenvironment in bladder cancer: the missing link. *Front Cell Dev Biol* 2021; **9**: 683940.

46. Guo CC, Bondaruk J, Yao H, *et al.* Assessment of luminal and basal phenotypes in bladder cancer. *Sci Rep* 2020; **10**: 9743.

47. Kamoun W, Swindell E, Pien C, *et al.* Targeting EphA2 in bladder cancer using a novel antibody-directed nanotherapeutic. *Pharmaceutics* 2020; **12**: 996.

48. Novruzov E, Dendl K, Ndlovu H, *et al.* Head-to-head intra-individual comparison of [^{68}Ga]-FAPI and [^{18}F]-FDG PET/CT in patients with bladder cancer. *Mol Imaging Biol* 2022; **24**: 651–658.

49. Zboralski D, Hoehne A, Bredenbeck A, *et al.* Preclinical evaluation of FAP-2286 for fibroblast activation protein targeted radionuclide imaging and therapy. *Eur J Nucl Med Mol Imaging* 2022; **49**: 3651–3667.

50. Casadei C, Dizman N, Schepisi G, *et al.* Targeted therapies for advanced bladder cancer: new strategies with FGFR inhibitors. *Ther Adv Med Oncol* 2019; **11**: 1758835919890285.

51. Patelli G, Zeppellini A, Spina F, *et al.* The evolving panorama of HER2-targeted treatments in metastatic urothelial cancer: a systematic review and future perspectives. *Cancer Treat Rev* 2022; **104**: 102351.

52. Koshkin VS, O'Donnell P, Yu EY, *et al.* Systematic review: targeting HER2 in bladder cancer. *Bladder Cancer* 2019; **5**: 1–12.

53. Rose TL, Chism DD, Alva AS, *et al.* Phase II trial of palbociclib in patients with metastatic urothelial cancer after failure of first-line chemotherapy. *Br J Cancer* 2018; **119**: 801–807.

54. Sjödahl G, Lövgren K, Lauss M, *et al.* Infiltration of CD3$^+$ and CD68$^+$ cells in bladder cancer is subtype specific and affects the outcome of patients with muscle-invasive tumors. *Urol Oncol* 2014; **32**: 791–797.

55. Warrick JI, Walter V, Yamashita H, *et al.* FOXA1, GATA3 and PPARγ cooperate to drive luminal subtype in bladder cancer: a molecular analysis of established human cell lines. *Sci Rep* 2016; **6**: 38531.

56. Robinson BD, Vlachostergios PJ, Bhinder B, *et al.* Upper tract urothelial carcinoma has a luminal-papillary T-cell depleted contexture and activated FGFR3 signaling. *Nat Commun* 2019; **10**: 2977.

57. Palmbos PL, Wang Y, Bankhead Iii A, *et al.* ATDC mediates a TP63-regulated basal cancer invasive program. *Oncogene* 2019; **38**: 3340–3354.

58. Naba A, Clauser KR, Hoersch S, *et al.* The matrisome: in silico definition and in vivo characterization by proteomics of normal and tumor extracellular matrices. *Mol Cell Proteomics* 2012; **11**: M111.014647.

59. Xue Y, Tong L, LiuAnwei Liu F, *et al.* Tumor-infiltrating M2 macrophages driven by specific genomic alterations are associated with prognosis in bladder cancer. *Oncol Rep* 2019; **42**: 581–594.

60. Gröger M, Holnthoner W, Maurer D, *et al.* Dermal microvascular endothelial cells express the 180-kDa macrophage mannose receptor in situ and in vitro. *J Immunol* 2000; **165**: 5428–5434.

61. Collin M, Bigley V. Human dendritic cell subsets: an update. *Immunology* 2018; **154**: 3–20.

62. Torsteinsdóttir I, Arvidson NG, Hällgren R, *et al.* Enhanced expression of integrins and CD66b on peripheral blood neutrophils and eosinophils in patients with rheumatoid arthritis, and the effect of glucocorticoids. *Scand J Immunol* 1999; **50**: 433–439.

63. Soehnlein O, Lindbom L. Neutrophil-derived azurocidin alarms the immune system. *J Leukoc Biol* 2009; **85**: 344–351.

64. van Acker HH, Capsomidis A, Smits EL, *et al.* CD56 in the immune system: more than a marker for cytotoxicity? *Front Immunol* 2017; **8**: 892.

65. Elosegui-Artola A, Andreu I, Beedle AEM, *et al.* Force triggers YAP nuclear entry by regulating transport across nuclear pores. *Cell* 2017; **171**: 1397–1410.e14.

66. Latz S, Umbach T, Goltz D, *et al.* Cytoplasmatic and nuclear YAP1 and pYAP1 staining in urothelial bladder cancer. *Urol Int* 2016; **96**: 39–45.

67. Elbediwy A, Vanyai H, Diaz-de-la-Loza M-D-C, *et al.* Enigma proteins regulate YAP mechanotransduction. *J Cell Sci* 2018; **131**: jcs221788.

68. Totaro A, Panciera T, Piccolo S. YAP/TAZ upstream signals and downstream responses. *Nat Cell Biol* 2018; **20**: 888–899.

69. Kiss B, Wyatt AW, Douglas J, *et al.* Her2 alterations in muscle-invasive bladder cancer: patient selection beyond protein expression for targeted therapy. *Sci Rep* 2017; **7**: 42713.

70. Stifano G, Christmann RB. Macrophage involvement in systemic sclerosis: do we need more evidence? *Curr Rheumatol Rep* 2016; **18**: 2.

71. Nakamura K, Okamura H, Wada M, *et al*. Endotoxin-induced serum factor that stimulates gamma interferon production. *Infect Immun* 1989; **57**: 590–595.

72. Yang J, Zhu H, Murphy TL, *et al*. IL-18-stimulated GADD45 beta required in cytokine-induced, but not TCR-induced, IFN-gamma production. *Nat Immunol* 2001; **2**: 157–164.

73. Hurst CD, Alder O, Platt FM, *et al*. Genomic subtypes of non-invasive bladder cancer with distinct metabolic profile and female gender bias in KDM6A mutation frequency. *Cancer Cell* 2017; **32**: 701–715.e7.

74. Shihab HA, Gough J, Cooper DN, *et al*. Predicting the functional, molecular, and phenotypic consequences of amino acid substitutions using hidden Markov models. *Hum Mutat* 2013; **34**: 57–65.

75. Landrum MJ, Lee JM, Benson M, *et al*. ClinVar: improving access to variant interpretations and supporting evidence. *Nucleic Acids Res* 2018; **46**: D1062–D1067.

76. Pataskar A, Champagne J, Nagel R, *et al*. Tryptophan depletion results in tryptophan-to-phenylalanine substitutants. *Nature* 2022; **603**: 721–727.

77. Bryan RT, Tselepis C. Cadherin switching and bladder cancer. *J Urol* 2010; **184**: 423–431.

78. Binder H, Schumacher M. Allowing for mandatory covariates in boosting estimation of sparse high-dimensional survival models. *BMC Bioinformatics* 2008; **9**: 14.

79. Szymanski KM, Binns D, Bartz R, *et al*. The lipodystrophy protein seipin is found at endoplasmic reticulum lipid droplet junctions and is important for droplet morphology. *Proc Natl Acad Sci U S A* 2007; **104**: 20890–20895.

80. Hothorn T, Lausen B. On the exact distribution of maximally selected rank statistics. *Comput Stat Data Anal* 2003; **43**: 121–137.

81. Uhlén M, Fagerberg L, Hallström BM, *et al*. Proteomics. Tissue-based map of the human proteome. *Science* 2015; **347**: 1260419.

82. Lánczky A, Győrffy B. Web-based survival analysis tool tailored for medical research (KMplot): development and implementation. *J Med Internet Res* 2021; **23**: e27633.

83. McCarty KS, Miller LS, Cox EB, *et al*. Estrogen receptor analyses. Correlation of biochemical and immunohistochemical methods using monoclonal antireceptor antibodies. *Arch Pathol Lab Med* 1985; **109**: 716–721.

84. Wallard MJ, Pennington CJ, Veerakumarasivam A, *et al*. Comprehensive profiling and localisation of the matrix metalloproteinases in urothelial carcinoma. *Br J Cancer* 2006; **94**: 569–577.

85. Davies B, Waxman J, Wasan H, *et al*. Levels of matrix metalloproteases in bladder cancer correlate with tumor grade and invasion. *Cancer Res* 1993; **53**: 5365–5369.

86. He B, Shi J, Wang X, *et al*. Label-free absolute protein quantification with data-independent acquisition. *J Proteomics* 2019; **200**: 51–59.

87. Wang J-F, Gong Y-Q, He Y-H, *et al*. High expression of MMP14 is associated with progression and poor short-term prognosis in muscle-invasive bladder cancer. *Eur Rev Med Pharmacol Sci* 2020; **24**: 6605–6615.

SUPPLEMENTARY MATERIAL ONLINE

Supplementary materials and methods

Figure S1. Proteome coverage; segregation of NMIBC and MIBC proteomes

Figure S2. Detected and differentially regulated proteins in treatment-naïve MIBC versus NMIBC involved in the KEGG pathway "Complement and coagulation cascade"

Figure S3. Detected and differentially regulated proteins in treatment-naïve MIBC versus NMIBC involved in the KEGG pathway "Focal adhesion"

Figure S4. Detected and differentially regulated proteins in treatment-naïve MIBC versus NMIBC involved in the KEGG pathway "Protein processing in the endoplasmic reticulum"

Figure S5. Proteomic similarity between treatment-naïve ($n = 51$) and neoadjuvant-treated ($n = 11$) MIBC based on proteomic profiles

Figure S6. Comparison of proteomic MIBC subgroups to published transcriptomic MIBC subgroups

Figure S7. Boxplots of selected therapeutic targets in bladder cancer

Figure S8. Upregulated proteins of the complement and coagulation cascade in the ECM subgroup according to KEGG pathway analysis

Figure S9. Expression levels of proteins associated with the transcriptional activity of YAP1 [74,75] in BC subgroups

Figure S10. Mass-spectrometric and immune-histochemical assessment of Ki-67

Figure S11. Analysis of tryptophan-phenylalanine-substitution across BC subtypes

Figure S12. Heatmap showing the results of searching the DIA data with a predicted spectral library

Figure S13. Mass-spectrometric and immune-histochemical assessment of BSCL2

Figure S14. Assessment of endogenous proteolysis by semi-tryptic DIA data analysis

Figure S15. Biological pathways identified through gene ontology analysis of the PDX proteomic data

Table S1. Characteristics and overview of cohort

Table S2. Overview of PDX specimens and corresponding proteomic data

Table S3. Peptide and protein abundance matrices of cohort

Table S4. Proteome differences between NMIBC and MIBC

Table S5. Proteome differences between NMIBC subtypes

Table S6. Proteome differences between MIBC subtypes

Table S7. Overview of genomic panel sequencing data

Table S8. Semi-tryptic data analysis